Dissolution behavior of Ag-doped antibacterial borosilicate glass powders blended into polypropylene

GUO, Ruixin, ZHAO, Zhengkun, DENG, Wei, OJOVAN, Michael, XU, Kai and CHAKRABARTI, Anirban

Dissolution behavior of Ag-doped antibacterial borosilicate glass powders blended into polypropylene

Ruixin Guo[a], Zhengkun Zhao[a,b], Wei Deng[c], Michael Ojovan[a,d], Kai Xu[a,*], Anirban Chakrabarti[a]

[a] State Key Laboratory of Silicate Materials for Architectures, Wuhan University of Technology, Wuhan 430070, P. R. China

[b] Anhui Zhenghe Materials Technology Co., Ltd, Chuzhou 239000, P. R. China

[c] College of Business, Technology and Engineering, Sheffield Hallam University, City Campus, Sheffield S1 1WB, UK

[d] School of Chemical, Materials and Biological Engineering, The University of Sheffield, Sheffield S10 2TN, UK

[*] Corresponding author

E-mail address: kaixu@whut.edu.cn (K. Xu).

Abstract:

Silver-doped borosilicate glass powders are frequently embedded into polymer matrices for potential antimicrobial applications. To assess the long-term release kinetics of Ag-containing borosilicate glass powder in polymer matrices, polypropylene (PP) blended with 5 wt% Ag-doped borosilicate glass powders was fabricated via the melt blending process. Additionally, immersion tests were conducted at 60 °C for up to 169 days under both dynamic (water flow rate ~220 mL/day) and static aqueous conditions. Notably, both boron (B) and sodium (Na) exhibited stable release (0.1–0.4 ppm) over 90 days under dynamic conditions. SEM analysis revealed near-complete dissolution of the glass adjacent to the surface (depth: ~0.2 mm), while the centrally embedded particles (depth: ~1.0 mm) remained largely intact. Under static conditions, the concentrations of B and Na increased parabolically up to day 76 and attained kinetic equilibrium by day 103. This was followed by linear increases (~83.9 ppm B, ~97.1 ppm Na by day 169), which correlated with the appearance of Na-rich flake-like precipitates. Although the congruent dissolution profiles of B and Na remained similar under both conditions, the slower rate under static conditions was attributed to limited water penetration within the PP matrix.

Keywords:

borosilicate glass, antibacterial glass, long-term dissolution behavior, PP, dynamic and static conditions

1. Introduction

The propagation of pathogens, along with their growing resistance to conventional antibiotics, has significantly raised global concern, driving research into antibacterial composite materials used alongside antibiotics in numerous cases [1–3]. One effective approach to achieving this goal is the incorporation of silver ion-containing glass into polymers. Shuai et al. [4] synthesized a polymer scaffold containing Ag-loaded mesoporous bioactive glasses, which exhibited robust antibacterial activity with over 99% bacterial inhibition rate against Escherichia coli attributed to the continuous release of Ag^+ ions. Moreover, the scaffold demonstrated good cytocompatibility in facilitating osteoblast adhesion and proliferation. Numaguchi et al. [5] fabricated a composite of polypropylene (PP) resin blended with 0.2–0.4 wt% of Ag-doped phosphate glass. Notably, this composite released Ag^+ ions in the range of 0.9–4.0 ng/(cm^2·day) and thus demonstrated an antibacterial activity of ≥2, as evaluated by JIS Z 2801:2000. Polymers containing antibacterial glass offer highly promising perspectives and have garnered significant interest in the fields of medical devices [6], food packaging [7], and electronics [8].

Silver-based antibacterial glass can release Ag^+ ions into the aqueous environment at a controlled rate, effectively inhibiting bacterial reproduction and growth through mechanisms such as bacterial protein deactivation and DNA degradation [9]. Currently, the precise modulation of tunable antibacterial metal ion release from the glass matrix remains a major challenge in optimizing the antibacterial activity of glass and its products. Guo et al. [10] demonstrated that generally, an increase in the Na/B molar ratio of glass composition reduces elemental release, including Ag^+ release profiles from borosilicate glasses within 12 hours, lowering antibacterial performance. Nevertheless, the governing dissolution mechanisms of silicate glasses involving both diffusion-controlled ion-exchange and glass network hydrolysis processes are known to change over time [11–13]. According to Gin et al. [14], re-polymerization of the silicon-oxygen network occurs on the surface layer of borosilicate glass immersed in silica-saturated solutions over extended periods of nearly

350 days. This forms a stable passivation layer adhered to the pristine glass surface, significantly decelerating elemental release rates. In particular, this glass dissolution behavior potentially limits the release of antibacterial ions, leading to the deterioration of the antibacterial activity of glass.

Although existing research has established fundamental relationships between glass composition, environmental conditions (e.g., temperature, solution saturation), and long-term dissolution behavior [15–17], few studies have investigated the dissolution behavior of glass powders incorporated into polymeric materials such as plastics. As reported by Jiang et al. [18], a 60-day aqueous immersion drastically reduced the antibacterial efficiency for plastic loaded with silver-based antibacterial glass, attributed to uncontrolled glass dissolution and Ag^+ release. Moreover, some studies have focused solely on the short-term (usually within one day) antibacterial activity of polymer containing antibacterial glasses, recording the Ag^+ release profiles from the glass-blended polymer in 24 h [4,5]. However, there are limitations to the extrapolation of these results to long-term service environments, primarily due to the lack of systematic studies of long-term behavior in polymer environments. Therefore, in this study, PP sheets embedded with silver-doped antibacterial borosilicate glass were fabricated to investigate the long-term element dissolution behavior along with the morphological alterations of the glass under simulated dynamic and static immersion conditions. The elemental release kinetics over extended durations (up to 169 days) were quantitatively monitored through dynamic and static immersion experiments, while characterizing morphological alterations at the glass-PP matrix interface using field emission scanning electron microscopy. Furthermore, the dissolution mechanisms of glass blended into the PP matrix under dynamic and static conditions were discussed.

2. Experimental

2.1. Sample preparation

In this study, Ag-doped antibacterial borosilicate glass particles with a mass composition of $30Na_2O$-$55B_2O_3$-$15SiO_2$ with an addition of 1 wt% Ag_2O were synthesized following the same method as described in our previous study [10]. Herein,

approximately 30 g of the glass particles (density: ~2.41 g/cm^3) were pulverized by planetary milling in a 500-mL nylon jar (containing ~60 g of zirconia balls with diameters ranging from 5 to 10 mm) at 300 rpm/min for 6 h using anhydrous ethanol as a disperse medium. The slurry was dried at 105 °C overnight and subsequently sieved through a 600-mesh sieve. After washing three times using anhydrous ethanol and drying process, the glass powders with an average size of approximately 12.0 μm were obtained, as examined by the laser particle size analyzer (LPSA, Malvern Instruments Ltd., Mastersizer 2000).

As part of the experimental process, 7.5 g of glass powder was blended into 142.5 g of the raw material polypropylene (commercial grade, PPD-MT20 from Sinopec Group Co., Ltd.) at a mass ratio of 5:95. The mixed materials were subsequently melt-compounded in a single-screw extruder (Haida HDX50). Furthermore, square blend sheets measuring 50×50×3 mm were prepared following extrusion and demolding. The temperatures in the four extruder zones were set to 230, 240, 240, and 230°C, respectively. The sheets were cut to remove peripheral edges, thus obtaining the central region of samples measuring 32×32×3 mm. The sample cross sections were polished under flowing anhydrous ethanol using sequential abrasive papers (800-, 1200-, and 2000-mesh grits). The polished specimens were cleaned and dried for subsequent experiments.

2.2. Dynamic dissolution experiment

As illustrated in Fig. 1a, the dynamic dissolution experiment was conducted to assess the dissolution behavior of glass blended into PP. The polished PP sheet was immersed in a 70-mL perfluoroalkoxy (PFA) reactor filled with 70 mL of ultrapure water (pH≈5.5). Because the density of PP (~0.9 g/cm^3) is lower than that of water, the complete submersion of the sample is ensured by anchoring it to a polytetrafluoroethylene (PTFE) plate at the bottom of the reactor using a PTFE thread. The PFA reactor containing the sample was placed in an oven at 60 ±1 °C. Ultrapure water was drawn from a reservoir and transferred at a steady flow rate of ~220 mL/d using a syringe pump (Norgren Kloehn, Model 55022). The experimental setup was adapted from a single-pass flow-through (SPFT) configuration commonly used in

ASTM C1662-18; however, the present work did not follow the ASTM C1662 test procedure, and the results are therefore reported as continuous flow-through experiments rather than standardized ASTM tests. The effluent from the reactor was continuously collected in a PFA bottle. All connections are made with PTFE tubing. The concentrations of Na and Si in the effluent collected at 10-day intervals from day 6 to day 66 and additionally on days 73, 80, and 90 were quantified using inductively coupled plasma-atomic emission spectroscopy (ICP-AES, ThermoFisher, IRIS Intrepid II XSP). Meanwhile, the concentrations of B and Ag were determined using inductively coupled plasma-mass spectrometry (ICP-MS, ThermoFisher, X II). The post-dissolution specimen was retrieved at day 90, ultrasonically cleaned in anhydrous ethanol, and dried for subsequent characterization. The transmittance of pre- and post-dissolution specimens was analyzed using UV-vis spectrophotometry (Shimadzu UV3600).

The post-dissolution specimens were cut to obtain two pieces of different sizes: 10×32×3 mm and 22×32×3 mm. The cross sections of the smaller specimen were polished using sequential abrasive papers (800-, 1200-, and 2000-mesh grits) under flowing anhydrous ethanol. This was followed by scratch removal using a polishing cloth under anhydrous diamond suspension. Furthermore, the morphology of the post-dissolution glass coated with Pt was characterized after cleaning and drying using field emission scanning electron microscopy (FE-SEM, JEOL, JSM-IT800) equipped with an Ultim Max 65 energy dispersive X-ray spectrometer (EDS), operated at an accelerating voltage of 5–15 kV. The morphology of the pre-dissolution glass blended into PP was characterized by the same route.

2.3. Static dissolution experiment

As shown in Fig. 1b, another polished PP sheet was immersed in a 70-mL PFA reactor filled with 70 mL of ultrapure water having a pH of approximately 5.5. Notably, the sample anchoring method and experimental temperature (60°C) were identical to those described in Section 2.2. At immersion times of 6, 16, 26, ..., 96, 103, 122, and 169 d, 2 mL of leachate was extracted from the reactor using a pipette for ICP-AES analysis, with subsequent replenishment of 2 mL of fresh ultrapure water into the

reactor. The post-dissolution sample was retrieved at day 169, cleaned, and dried for subsequent characterization. Three additional polished PP sheets were subjected to identical experimental protocols, with immersion durations of 36, 71, and 103 days. Furthermore, a blank test for a neat PP sheet was conducted under the same protocols with an immersion duration of 169 days.

The morphological evolutions of the post-dissolution glasses in the four PP specimens were characterized using the same protocol described in Section 2.2.

3. Results and discussion

3.1. Glass dissolution behavior under dynamic conditions

3.1.1. Sample images and element release behavior

Fig. 2 presents the photos and transmittance spectra of pre- and post-dissolution samples. As depicted in Fig. 2, the neat PP (Fig. 2b) was transparent, whilst the transmittance of the PP sheet decreased after incorporating 5 wt% glass powders (Fig. 2c). This reduction is attributed to the strong surface plasmon resonance absorption of Ag^0 clusters around 420 nm dispersed in the glass [10] and the potential difference in the refractive index between PP and glass powders. The glass-blended PP sheets turned opaque (Fig. 2f) after 90 days of dynamic immersion, and a drastic decline of transmittance above 450 nm was recorded, although the neat PP sheet barely showed the loss (<5%) of transmittance.

The element leaching behavior of glass powders blended into the PP sheet was analyzed as a function of time under dynamic conditions using ICP-AES and MS. As depicted in Fig. 3, the element concentrations of B and Na in the leachate, the principal components of glass, remained within 0.1–0.4 ppm throughout the 90-day immersion period. Notably, the mean element concentrations of Si and Ag in the leachate were below analytical significance (<0.08 ppm and <0.01 ppb, respectively) and thus omitted from the graphical representation.

The normalized dissolution rate of glass powders was calculated using the following equations:

$$rate = \frac{[C_i - C_i°] \times (\frac{F}{S°})}{f_i} \quad (1)$$

$$C_{Ag}{}^{*} = \frac{C_B}{f_B} \times f_{Ag} \quad (2)$$

Here, C_i represents the steady-state concentration of component i measured in the effluent solution (g/L), $Ci°$ denotes the background concentration of component i in the influent solution measured in a blank test (g/L), F denotes the solution flow rate (L/s), $S°$ represents the surface area of the PP sheet that is exposed to solution (m^2), which is 2.43×10^{-3} m^2. f_i denotes the mass fraction of component i in the glass. As shown in Fig. 3 and discussed in our previous work [10], the glass has a congruent dissolution behavior, leading to a similar normalized concentration of B and Ag in the leachate. $C_{Ag}{}^{*}$, the estimated concentration of Ag in the effluent solution, could be calculated following the Eq. (2). The calculation result of the normalized dissolution rate of B is found to be 1.20×10^{-6} g/(m^2·s), which likely represents the dissolution rate of glass powders owing to a higher content of glass former B than Si. Notably, the dissolution rate of glass powders in the PP matrix was extremely low, which is in a similar level to the durable glass system as shown in [19]. This indicates improved chemical durability of antibacterial glass powders blended into the PP matrix, which acts as a barrier to water penetration [20]. According to the antibacterial activity test by JIS Z 2801:2000 [5], the preferable range for Ag release is 0.58–11.57×10^{-10} g/(m^2·s). The estimated concentration of Ag release from the glass powders was 0.011 ppm calculated by Eq. (2) and the estimated Ag release rate was similar to that of B, highlighting the potential antibacterial performance of the PP sample. However, the actual Ag concentration in the leachate was <0.01 ppb, significantly lower than the estimated concentration. This might be attributed to the dispersion of Ag^0 clusters in the glass system as discussed in our previous study [10] and the complexity of PP matrix.

3.1.2. Morphological evolutions of pre- and post-dissolution glass

FE-SEM images before immersion revealed the distribution of glass powders blended into the PP matrix (Fig. 4a). EDS analysis shown in Fig. 4b confirmed that the elemental contents of pre-dissolution glass maintained stoichiometry equivalent to the

nominal composition, while the PP substrate comprised 100 wt% of the element C. It should be noted that EDS analysis cannot detect another element, H, in the PP substrate.

Notably, significant morphological evolution occurred following 90-d dynamic immersion. As shown in Fig. 4c, the morphological changes in the cross section of post-dissolution glass from the two regions at approximately 0.2 and 1.0 mm beneath the surface of the PP sheet were investigated using FE-SEM. Fig. 4d displays residual glass fragments or dissolution products smaller than 1 μm at a depth of approximately 0.2 mm lying on the PP substrate, containing less than 1 wt% of Na and Si, which is considerably lower than their pre-dissolution contents. This near-complete elemental depletion indicated massive glass dissolution in near-surface regions. The glass particles retained macroscopic integrity at a depth of approximately 1.0 mm but exhibited pitted surfaces with similar preferential leaching features [21], as depicted in Fig. 4g. The glass powder at a greater depth of approximately 1.1 mm in Fig. 4h retained higher shape integrity than that in Fig. 4f, indicating less alteration of glass. Moreover, EDS analysis in Fig. 4f demonstrated the following: (i) boron depletion—the B content in the post-dissolution glass fell below detection limits, confirming boron dissolution; (ii) a decrease in the sodium-silicon (Na/Si) molar ratio—the molar ratio of Na/Si decreased from approximately 3.56 (pre-dissolution) to 0.56 (post-dissolution), indicating preferential leaching of Na over Si; and (iii) absence of passivation—the Si-rich gel layer, typically associated with limited mass diffusion and glass alteration [14], was absent at the surface of the glass, consistent with the near-constant elemental release profiles from the glass powder (Fig. 3). The dissolution of glass powders inside the PP matrix, resulting in severe disruption of glass optical properties and accumulation of dissolution byproducts, consequently decreasing the transmittances of glass and the PP matrix (Fig. 2).

3.2. Glass dissolution behavior under static conditions

3.2.1 Elemental release behavior

As depicted in Fig. 5a, the concentrations of B and Na evolved through three distinct stages over time: (1) the initial dissolution and rate drop—rapid concentration surges were observed within the first 6 days, with B and Na concentrations approaching

approximately 15.4 and 20.1 ppm, respectively. A subsequent gradual deceleration in glass dissolution led to increased concentrations of ~50.4 ppm (B) and ~56.4 ppm (Na) at day 76. The fitted element concentration-time curves of B and Na were generally close to $C=kt^{1/2}$ (C: the element concentration in solution, t: time, k: a coefficient related to diffusion-controlled ion-exchange) following parabolic behavior, indicating diffusion-controlled kinetics of glass dissolution [11–13] followed by the formation of alteration layers [15]. (2) The residual rate stage, where both elements exhibited stabilized leaching profiles, implying potential quasi-equilibrium between glass dissolution and mass transport kinetics. (3) A stable and relatively rapid alteration, as element concentrations resumed a linear upward trajectory, reaching approximately 83.9 ppm (B) and ~97.1 ppm (Na) by day 169, reflecting the hydrolytic nature of glass network dissolution characteristic of the late stages of glass corrosion in aqueous systems [22–24]. Notably, since the concentrations of Si and Ag remained below analytical significance (the average values: <1 ppm and <6 ppb, respectively), they were omitted from the graphical representation. The pH of the leachate measured using a pH meter (SMART SENSOR PH8008), was around 8.0 during 6−81 d of immersion. It could be assumed that the pH throughout the experiment had little change due to the low release of Na in the leachate.

Following the standard test protocol (the product consistency test, PCT) ASTM C1285-02 for evaluating the chemical durability of glasses, the normalized release rates of element B and Na were calculated as follows:

$$NR_i = \frac{C_i}{f_i \cdot (S°/V) \cdot t} \tag{3}$$

Here, NR_i represents the normalized release rate of component i, C_i denotes the concentration of component i measured in the leachate (g/L), f_i represents the mass fraction of component i in the glass, $S°/V$ denotes the surface area of the PP sheet $S°$ (m^2) divided by the leachate volume V (L), and t denotes the time duration of test (s). The calculated normalized release rates of B was 5.04×10^{-6} g/(m^2·s) at 6 d, which significantly decreased to 1.31×10^{-6} g/(m^2·s) by day 76 and gradually stabilized at a value of 9.70×10^{-7} g/(m^2·s) during the period between days 103 and 169 (Fig. 5b). The

release kinetics of Na exhibited an analogous result, suggesting the congruent dissolution of glass under static conditions.

3.2.2 Morphological evolutions of post-dissolution glass

Fig. 6 displays the SEM images and EDS analysis of post-dissolution glass at a depth of approximately 1 mm beneath the surface of the PP matrix at different duration times. A clear shape of glass powders was recorded after immersion for 36–169 days (Fig. 6a–d). As indicated in Fig. 6e–f, glass particles exhibited extensive surface pitting after 36 and 71 days, consistent with the selective leaching features observed under dynamic conditions in Fig. 4g. EDS analysis revealed potential boron depletion (below detection limits) and a reduced molar ratio of Na/Si (Fig. 7) from approximately 3.56 (pre-dissolution) to 1.44 (post-dissolution at 36 d) in the alteration layers, confirming preferential leaching of B and Na over Si. This resulted in Si enrichment in the alteration layers of glass powders. Furthermore, flake-like phases massively formed on the glass surface by day 103, characterized by Na-rich and Si-poor compositions with an increased Na/Si ratio of nearly 8.69. It can be assumed that Na-rich secondary precipitate phases formed on the glass surface, aligning with the literature [25]. The flake-like precipitates disappeared by day 169, occurring alongside the generation of glass debris smaller than 1 μm and a decreased Na/Si ratio of approximately 0.36. These features indicate accelerated glass dissolution.

3.3. Dissolution mechanisms of glass blended into PP

The dissolution behavior of glass blended into PP was regulated by two distinct mechanisms under dynamic and static conditions. As evidenced by the elemental leaching profiles in Fig. 3, both B and Na demonstrated stable dissolution kinetics over the 90-d immersion, suggesting congruent dissolution behavior of glass under both dynamic conditions and static conditions (Fig. 5). The dynamic aqueous condition facilitates continuous mass transport: fresh ultrapure water permeates into the PP matrix while dissolution byproducts are simultaneously transported outward via aqueous efflux [18,26]. This mechanism effectively suppressed localized accumulation of dissolved species in the vicinity of glass powders, thereby preventing passivation layer formation at the glass surface [27]. Consequently, the sustained chemical potential

gradient between the glass and bulk solution facilitated the forward progression of glass dissolution reactions.

Despite being dispersed within the PP matrix, the glass powder exhibited three stages of dissolution kinetics accompanied by corresponding morphological evolutions under static conditions. This behavior is analogous to that of the nuclear waste borosilicate glass, which is commonly recognized as corrosion-resistant under conventional conditions of natural waters [14,15,23,28]. During the initial stage of dissolution (under pseudo-infinite dilution conditions), the rate dropped due to diffusion-controlled ion release kinetics from glass. At this stage, water penetration through the PP matrix became the dissolution rate-limiting process [15], owing to slower water penetration compared to ion diffusion in water [18]. As depicted in Fig. 5, near-zero concentrations of B and Na in interfacial water possessed maximal chemical potential gradients in the early stage, driving progressive glass dissolution. This led to the gradual accumulation of dissolved species in the vicinity of glass, reducing hydrolytic dissolution rates (Fig. 5b) [29], accompanied by the pitting morphology (Fig. 6e–f).

The concentrations of B and Na in the vicinity of the glass reached a near-constant level as immersion time prolonged to 76 days. This corresponds to the decreasing dissolution rate of glass (Fig. 5b) and establishes potential dynamic equilibrium between the kinetics of hydrolytic dissolution of glass and water penetration through the PP matrix [15]. This metastable condition temporarily stabilized both dissolution rates and surface morphology at the residual rate stage. After 103 days, an extended hydrothermal exposure likely induced degradation of the PP matrix [30] and glass powders, thus increasing the porosity of samples, accompanied by the enhancement of water penetration. This disrupts prior dynamic equilibrium, triggering precipitation of Na-rich secondary phases (Fig. 6g) and driving the forward progression of glass dissolution reactions following linear kinetics (Fig. 5a). Nevertheless, the dissolution behavior of glass powders blended into the PP matrix is influenced by other factors, including the distribution of glass powders, local pH evolution and potential PP matrix swelling, which will be investigated in future work.

4. Conclusions

In conclusion, two distinct glass dissolution behaviors were observed for glass powders blended into the PP matrix under dynamic and static aqueous conditions. Under dynamic aqueous conditions, stable elemental dissolution rates of 1.20×10^{-6} g/(m^2·s) for B were observed across immersion durations. After 90 days, glass powders in the surface layer (depth <0.2 mm) underwent near-complete dissolution, whereas those in the inner area (depth >1 mm) experienced limited dissolution. Furthermore, enhanced water penetration at the PP matrix under flowing conditions facilitated the forward progression of glass dissolution reactions and prevented any passivation layer formation on the glass surface. Under static immersion, initial rapid dissolution and rate drop for the initial stage (0–76 d) transitioned to potential kinetic equilibrium (76–103 d). This was followed by Na-rich secondary precipitation and resumed linear dissolution with a steady dissolution rate of 9.70×10^{-7} g/(m^2·s) for B (103–169 d). Moreover, a lower steady dissolution rate for B from the glass powder in the PP matrix was obtained under static conditions, thus verifying reduced water penetration. To ensure long-term antibacterial efficacy across diverse service environments, compositional optimization of antibacterial glass blended into PP or other polymeric substrates must prioritize the release kinetics of antibacterial agents for long-term monitoring under diverse conditions.

Acknowledgements

The authors gratefully acknowledge the project of Science and Technology Plan (Grant No. 2022CX006) from Chuzhou government.

Reference

[1] Y.K. Cheong, J. Calvo-Castro, L. Ciric, M. Edirisinghe, E. Cloutman-Green, U.E. Illangakoon, Q. Kang, S. Mahalingam, R.K. Matharu, R.M. Wilson, G. Ren, Characterisation of the chemical composition and structural features of novel antimicrobial nanoparticles, Nanomaterials 7 (2017) 152.

https://doi.org/10.3390/nano7070152.

[2] R.K. Matharu, L. Ciric, G. Ren, M. Edirisinghe, Comparative study of the antimicrobial effects of tungsten nanoparticles and tungsten nanocomposite fibres on hospital acquired bacterial and viral pathogens, Nanomaterials 10 (2020) 1017. https://doi.org/10.3390/nano10061017.

[3] H. Haidari, K. Vasilev, Novel antibacterial materials and coatings—a perspective by the editors, Materials 16 (2023) 6302. https://doi.org/10.3390/ma16186302.

[4] C. Shuai, Y. Xu, P. Feng, G. Wang, S. Xiong, S. Peng, Antibacterial polymer scaffold based on mesoporous bioactive glass loaded with in situ grown silver, Chem. Eng. J. 374 (2019) 304–315. https://doi.org/10.1016/j.cej.2019.03.273.

[5] M. Numaguchi, M. Nomura, Antibacterial glass composition and antibacterial polymer composition using the same, US6939820B2, 2005. https://patents.google.com/patent/US6939820B2/en (accessed June 24, 2025).

[6] S. Saidin, M.A. Jumat, N.A.A. Mohd Amin, A.S. Saleh Al-Hammadi, Organic and inorganic antibacterial approaches in combating bacterial infection for biomedical application, Mater. Sci. Eng., C Mater. Biol. Appl. 118 (2021) 111382. https://doi.org/10.1016/j.msec.2020.111382.

[7] D. Olmos, J. González-Benito, Polymeric materials with antibacterial activity: a review, Polymers 13 (2021) 613. https://doi.org/10.3390/polym13040613.

[8] S. Ippili, J.-S. Jung, A.M. Thomas, V.-H. Vuong, J.-M. Lee, M.S. Sha, K.K. Sadasivuni, V. Jella, S.-G. Yoon, An overview of polymer composite films for antibacterial display coatings and sensor applications, Polymers 15 (2023) 3791. https://doi.org/10.3390/polym15183791.

[9] J.S. Fernandes, P. Gentile, R.A. Pires, R.L. Reis, P.V. Hatton, Multifunctional bioactive glass and glass-ceramic biomaterials with antibacterial properties for repair and regeneration of bone tissue, Acta Biomater. 59 (2017) 2–11. https://doi.org/10.1016/j.actbio.2017.06.046.

[10] R. Guo, Z. Zhao, C. Niu, H. Li, Effect of the ratio of R =[Na_2O]/[B_2O_3] on the structure, Ag species, and antibacterial activity of Ag-doped borosilicate glass, J. NonCryst. Solids 588 (2022) 121610.

https://doi.org/10.1016/j.jnoncrysol.2022.121610.

[11] V.V. Poluektov, V.A. Petrov, M.I. Ojovan, S.V. Yudintsev, Uranium retention in silica-rich natural glasses: nuclear waste disposal aspect, Ceramics 6 (2023) 1152–1163. https://doi.org/10.3390/ceramics6020069.

[12] M.I. Ojovan, On alteration rate renewal stage of nuclear waste glass corrosion, MRS Adv. 5 (2020) 111–120. https://doi.org/10.1557/adv.2020.36.

[13] M.I. Ojovan, A. Pankov, W.E. Lee, The ion exchange phase in corrosion of nuclear waste glasses, J. Nucl. Mater. 358 (2006) 57–68. https://doi.org/10.1016/j.jnucmat.2006.06.016.

[14] S. Gin, P. Jollivet, M. Fournier, F. Angeli, P. Frugier, T. Charpentier, Origin and consequences of silicate glass passivation by surface layers, Nat. Commun. 6 (2015) 6360. https://doi.org/10.1038/ncomms7360.

[15] G.S. Frankel, J.D. Vienna, J. Lian, J.R. Scully, S. Gin, J.V. Ryan, J. Wang, S.H. Kim, W. Windl, J. Du, A comparative review of the aqueous corrosion of glasses, crystalline ceramics, and metals, Npj Mater. Degrad. 2 (2018) 15. https://doi.org/10.1038/s41529-018-0037-2.

[16] N. Stone-Weiss, H. Bradtmüller, H. Eckert, A. Goel, Composition–Structure–Solubility Relationships in Borosilicate Glasses: Toward a Rational Design of Bioactive Glasses with Controlled Dissolution Behavior, ACS Appl. Mater. Interfaces 13 (2021) 31495–31513. https://doi.org/10.1021/acsami.1c07519.

[17] J.D. Vienna, J.J. Neeway, J.V. Ryan, S.N. Kerisit, Impacts of glass composition, pH, and temperature on glass forward dissolution rate, Npj Mater. Degrad. 2 (2018) 1–12. https://doi.org/10.1038/s41529-018-0042-5.

[18] Jiang Z. Studies on release kinetics of inorganic antimicrobial. Beijing, Technical Institute of Physics and Chemistry CAS, 2007. (In Chinese)

[19] Neeway, J.; Asmussen, R.; Parruzot, B.; Cordova, E.; Williams, B.; Leavy, I.; Stephenson, J.; Mcelroy, E. FY2016 ILAW Glass Corrosion Testing with the Single-Pass Flow-Through Method, PNNL-26169, Pacific NorthwestNational Laboratory, Richland, WA, 2017.

[20] C. Yang, X. Xing, Z. Li, S. Zhang, A comprehensive review on water diffusion in

polymers focusing on the polymer–metal interface combination, Polymers 12 (2020) 138. https://doi.org/10.3390/polym12010138.

[21] H. Takebe, Y. Baba, M. Kuwabara, Dissolution behavior of $ZnO–P_2O_5$ glasses in water, J. NonCryst. Solids 352 (2006) 3088–3094. https://doi.org/10.1016/j.jnoncrysol.2006.04.002.

[22] Q. Qin, N. Stone-Weiss, T. Zhao, P. Mukherjee, J. Ren, J.C. Mauro, A. Goel, Insights into the mechanism and kinetics of dissolution of aluminoborosilicate glasses in acidic media: Impact of high ionic field strength cations, Acta Mater. 242 (2023) 118468. https://doi.org/10.1016/j.actamat.2022.118468.

[23] S. Gin, X. Beaudoux, F. Angéli, C. Jégou, N. Godon, Effect of composition on the short-term and long-term dissolution rates of ten borosilicate glasses of increasing complexity from 3 to 30 oxides, J. NonCryst. Solids 358 (2012) 2559–2570. https://doi.org/10.1016/j.jnoncrysol.2012.05.024.

[24] T. Geisler, L. Dohmen, C. Lenting, M.B.K. Fritzsche, Real-time in situ observations of reaction and transport phenomena during silicate glass corrosion by fluid-cell Raman spectroscopy, Nat. Mater. 18 (2019) 342–348. https://doi.org/10.1038/s41563-019-0293-8.

[25] T.L. Goût, J.N.P. Lillington, J. Walden, C. Boukouvala, E. Ringe, M.T. Harrison, I. Farnan, Aqueous dissolution of Li-Na borosilicates: Insights from machine learning and experiments, J. NonCryst. Solids 621 (2023) 122630. https://doi.org/10.1016/j.jnoncrysol.2023.122630.

[26] A.E. Krauklis, H.A. Aouissi, S. Bencedira, J. Burlakovs, I. Zekker, I. Bute, M. Klavins, Influence of environmental parameters and fiber orientation on dissolution kinetics of glass fibers in polymer composites, J. Compos. Sci. 6 (2022) 210. https://doi.org/10.3390/jcs6070210.

[27] Y. Inagaki, T. Kikunaga, K. Idemitsu, T. Arima, Initial Dissolution Rate of the International Simple Glass as a Function of pH and Temperature Measured Using Microchannel FlowThrough Test Method, Int. J. Appl. Glass Sci. 4 (2013) 11.

[28] X. Guo, S. Gin, P. Lei, T. Yao, H. Liu, D.K. Schreiber, D. Ngo, G. Viswanathan, T. Li, S.H. Kim, J.D. Vienna, J.V. Ryan, J. Du, J. Lian, G.S. Frankel, Self-

accelerated corrosion of nuclear waste forms at material interfaces, Nat. Mater. 19 (2020) 310–316. https://doi.org/10.1038/s41563-019-0579-x.

[29] J.P. Icenhower, B.P. McGrail, W.J. Shaw, E.M. Pierce, P. Nachimuthu, D.K. Shuh, E.A. Rodriguez, J.L. Steele, Experimentally determined dissolution kinetics of Na-rich borosilicate glass at far from equilibrium conditions: Implications for Transition State Theory, Geochim. Cosmochim. Ac. 72 (2008) 2767–2788. https://doi.org/10.1016/j.gca.2008.02.026.

[30] N. Hamour, A. Boukerrou, H. Djidjelli, J.-E. Maigret, J. Beaugrand, Effects of MAPP compatibilization and acetylation treatment followed by hydrothermal aging on polypropylene alfa fiber composites, Int. J. Polym. Sci. 2015 (2015) 451691. https://doi.org/10.1155/2015/451691.

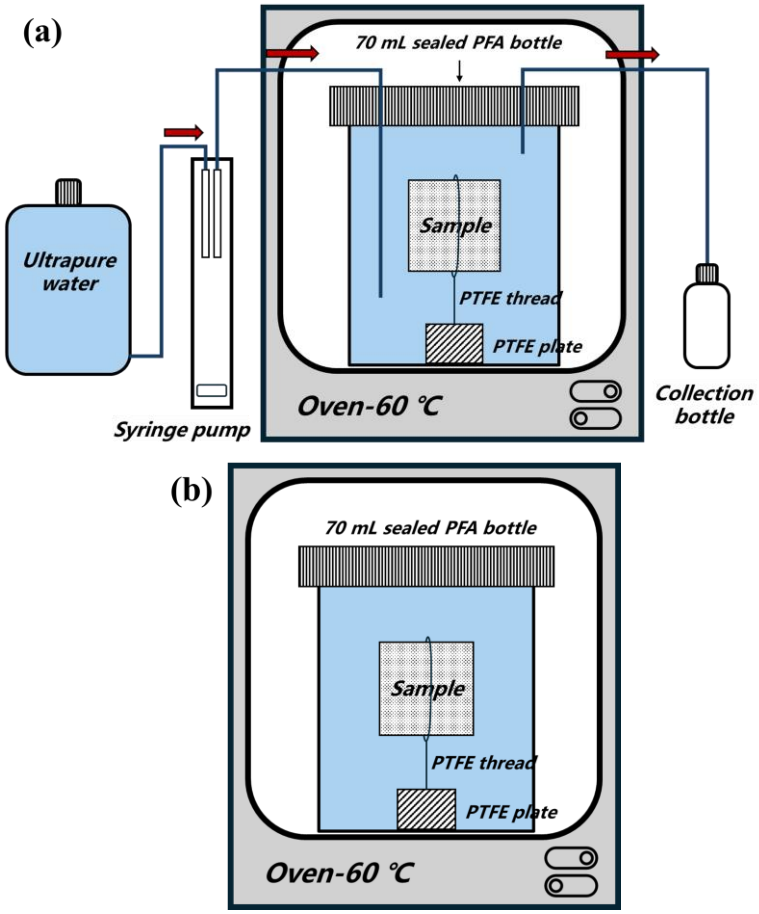

Fig. 1 Schematics of (a) dynamic and (b) static dissolution experiments.

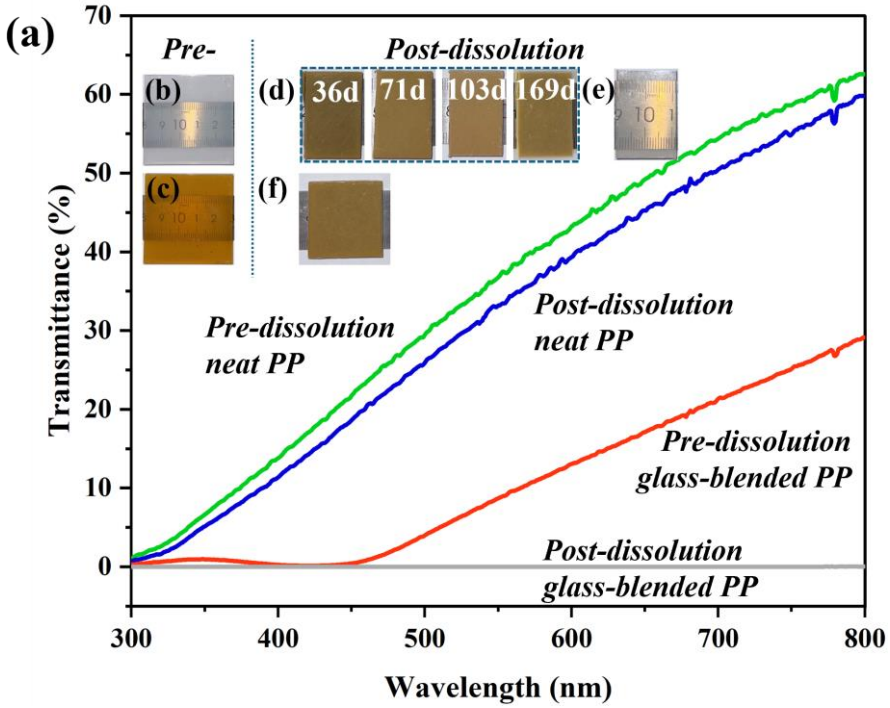

Fig. 2 Photos and transmittance spectra of samples. (a) The transmittance spectra in the range of 300–800 nm of samples: pre-dissolution neat PP (green line), post-dissolution neat PP at 169 d under static conditions (blue line), pre-dissolution glass-blended PP (red line), post-dissolution glass-blended PP at 36 d under static conditions (grey line). Photos of (b) pre-dissolution neat PP and (c) pre-dissolution glass-blended PP. (d) Photos of post-dissolution glass-blended PP sheets under static conditions at 36, 71, 103, and 169 d. (e) Photo of post-dissolution neat PP sheet at 169 d under static conditions. (f) Photo of post-dissolution glass-blended PP sheet at 90 days under dynamic conditions.

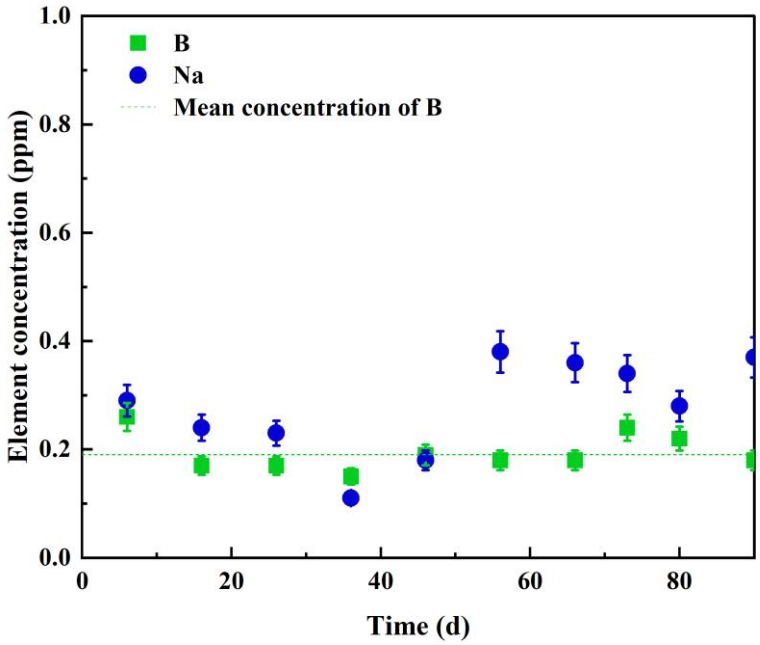

Fig. 3 Concentrations of B and Na in the leachate as a function of time under dynamic conditions. The dashed line shows the mean concentration of B.

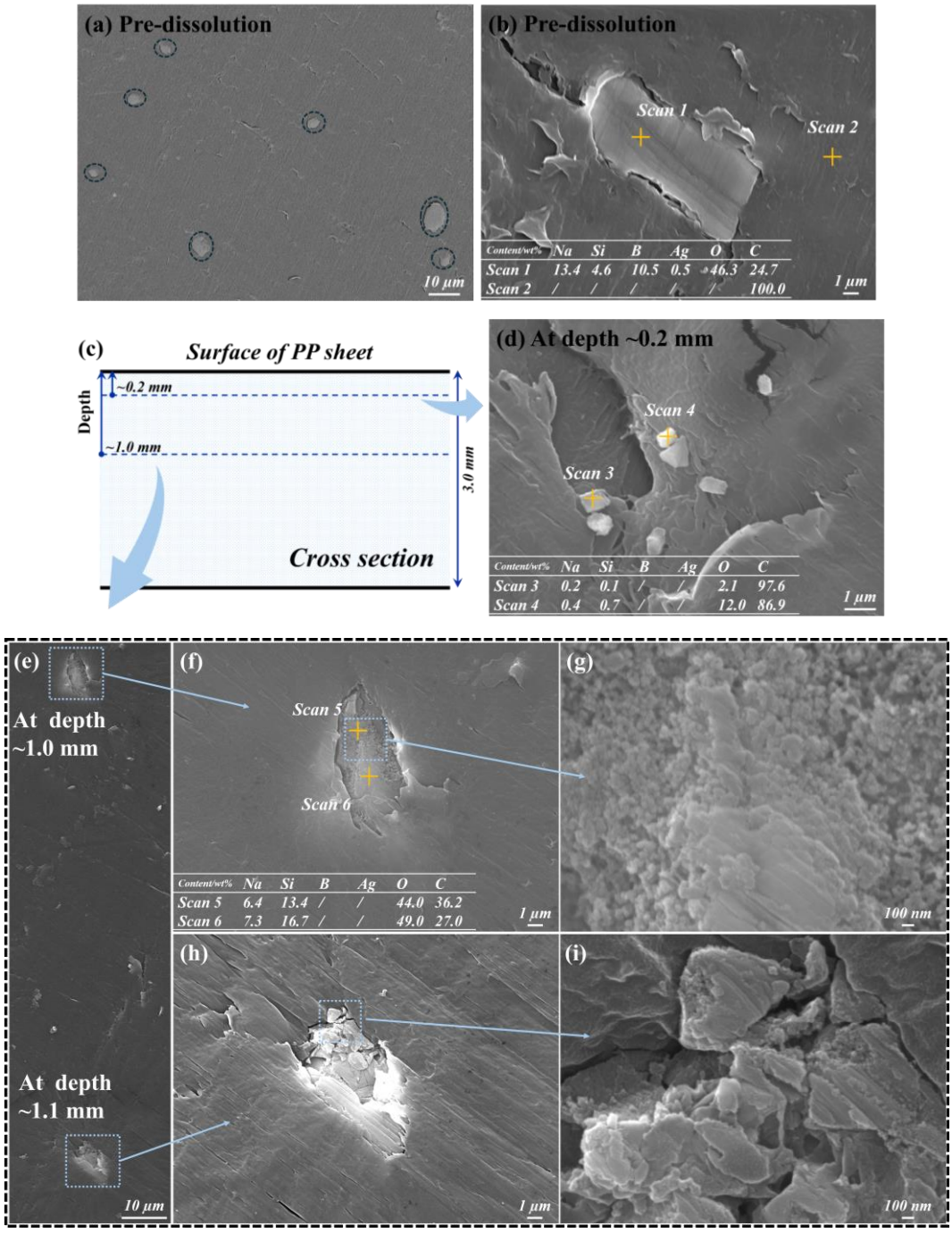

Fig. 4 SEM images and EDS data on the cross section of pre- and post-dissolution glasses. (a) SEM image of pre-dissolution glass. (b) SEM image and EDS data of pre-dissolution glass. (c) Schematic of scanning area in cross-section of sample for SEM-EDS. SEM images and EDS data of post-dissolution glass (d) near 0.2 mm and (e) 1.0–1.1 mm beneath the PP plate surface under dynamic conditions. (f) and (h) represent the magnified images of upper and lower glass particles, respectively. (g) and (i) represent the magnification of (f) and (h), respectively.

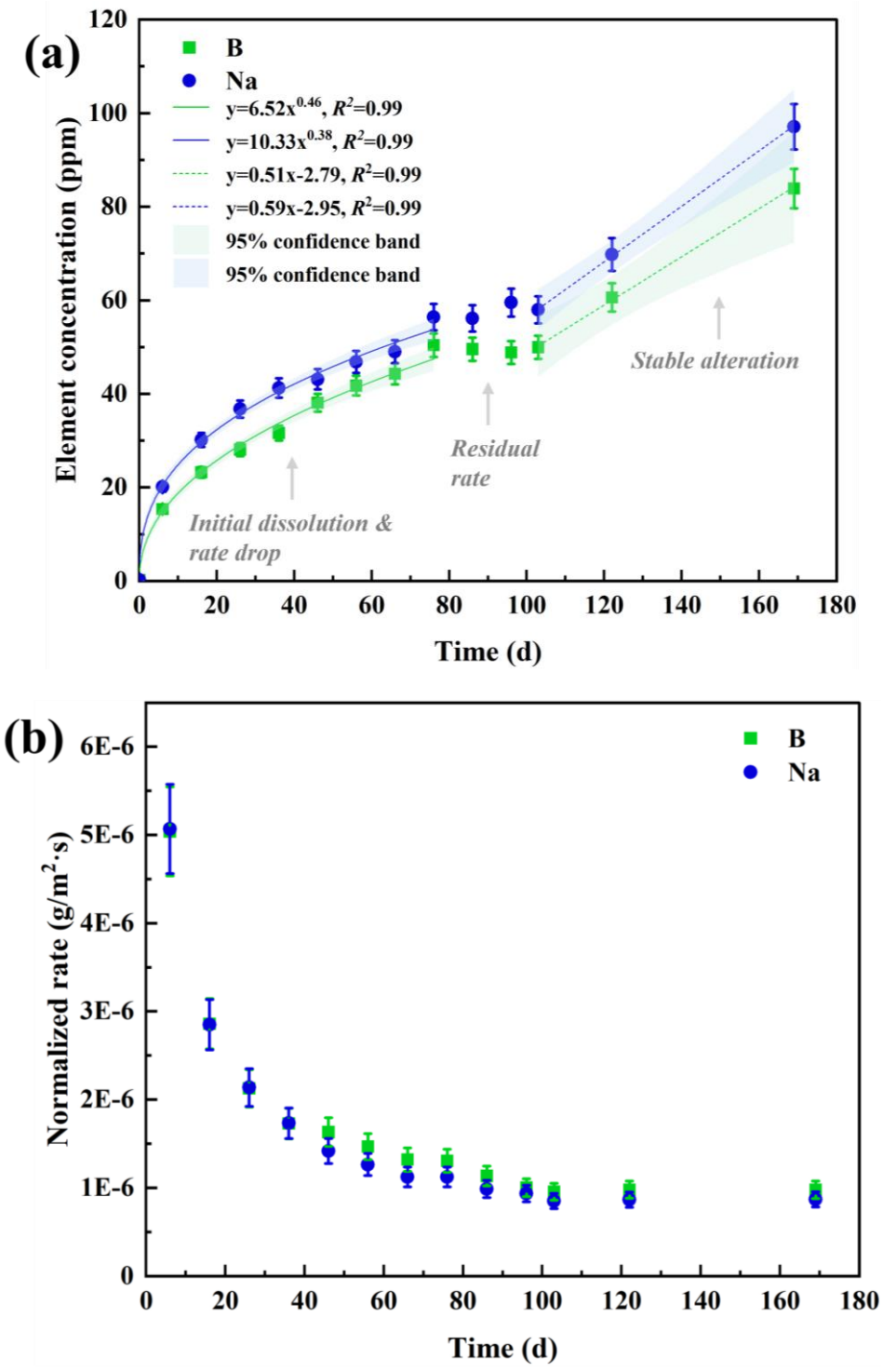

Fig. 5 (a) Element release and (b) Normalized rate of B and Na in the leachate of the sample as a function of time under static conditions. The solid and dashed lines in (a) represent Allometric 1 and Linear fittings with 95% confidence bands, respectively.

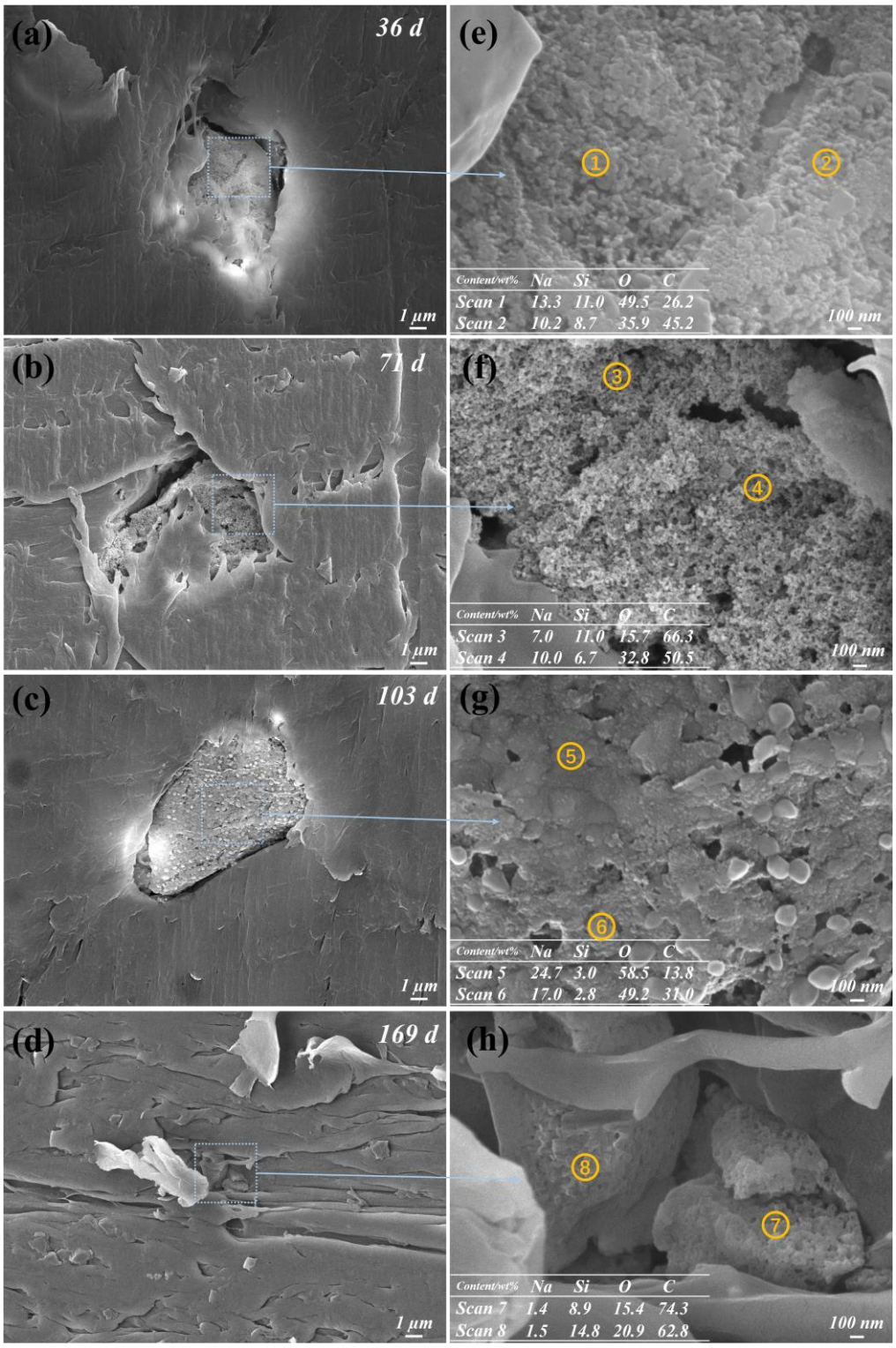

Fig. 6 SEM images of post-dissolution glass at (a) 36, (b) 71, (c) 103, and (d) 169 days under static conditions. (e)–(h) at the right side represents the magnified images with the insets of EDS data, respectively. The contents of B and Ag are under the detection limits of EDS.

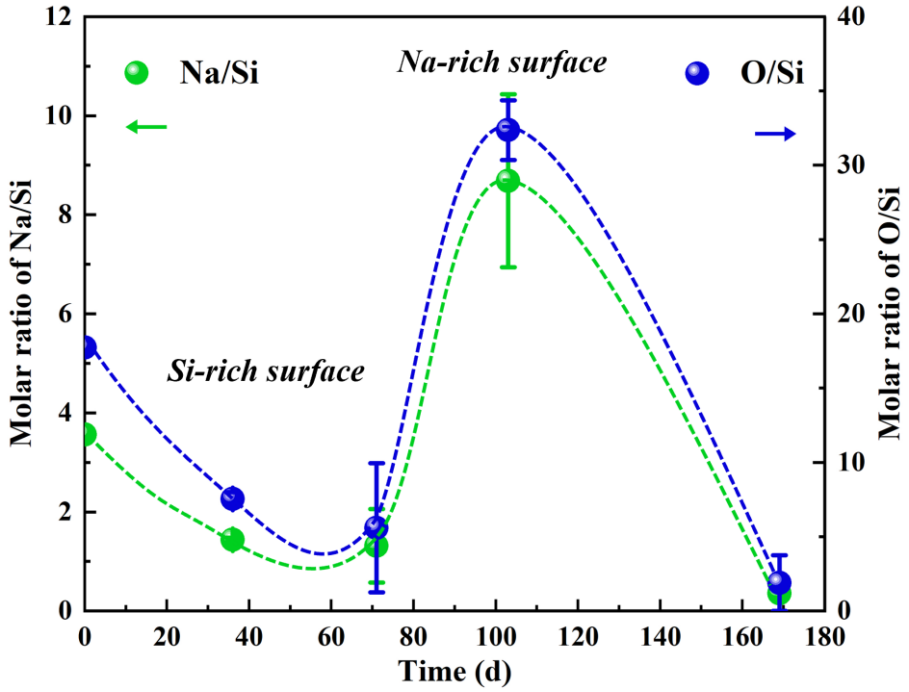

Fig. 7 Molar ratios of O/Si and Na/Si calculated from the result of EDS analysis as a function of time under static conditions. The dashed lines represent the trend line.